



Picosecond laser-induced surface structures on alloys in liquids and their influence on nanoparticle productivity during laser ablation

RUKSAN NADARAJAH, STEPHAN BARCIKOWSKI, AND BILAL GÖKÇE* 

University of Duisburg-Essen, Technical Chemistry I and Center for Nanointegration Duisburg-Essen (CENIDE), Universitätsstr. 7, 45141 Essen, Germany

*bilal.goekce@uni-due.de

Abstract: The productivity of nanoparticles formed by laser ablation of gold-silver and iron-gold alloy as well as copper and iron-nickel alloy targets in water is correlated with the formation of laser-induced surface structures. At a laser fluence optimized for maximum nanoparticle productivity, it is found that a binary alloy with an equimolar ratio forms laser-induced periodic surface structures (LIPSS) after ablation, if one of the constituent metals also form LIPSS. The ablation rate of nanoparticles linearly depends on the laser fluence if LIPSS is not formed, while a logarithmic trend and a decrease in productivity is evident when LIPSS is formed. To cancel LIPSS formation and recover from this decrease, a change to circularly polarized light is performed and an increase in nanoparticle productivity of more than 30% is observed.

© 2020 Optical Society of America under the terms of the [OSA Open Access Publishing Agreement](#)

1. Introduction

Laser ablation offers a broad application platform, which can be used for generating colloidal nanoparticles [1,2] and/or to induce surface structures such as “Laser induced periodic surface structures” (LIPSS) or ripples [3–7]. Surfaces with LIPSS have high potential in various mechanical, optical or medical applications, such as tribology [8,9], cellular growth manipulation [10], surface-enhanced Raman scattering detection [11], wettability control [12], and catalysis [13]. However, precise control of LIPSS structures is limited as the formation mechanism is still not fully understood [3]. It is known, that different parameters such as the irradiation wavelength, the angle of incidence, the polarization state, the laser peak fluence, the number of pulses applied to the irradiated spot, and the refractive index of the ambient medium play an important role for the formation of LIPSS [3,14,15]. LIPSS can be differentiated between high spatial frequency LIPSS (HSFL) and low spatial frequency LIPSS (LSFL). LSFLs have periodicity close to the laser wavelength, and are typical for continuous and nanosecond pulsed lasers, whereas HSFLs have a periodicity smaller than half of the incoming laser wavelength and are generated by ultrafast lasers such as femto- and picosecond lasers. Keilmann et al. developed the first theory with which they explained the LSFLs with optical interference of the incident laser radiation with surface plasmon polaritons [16]. Sipe et al. further introduced a mathematical formalism to describe the inhomogeneous energy deposition into the irradiated material [17]. But this mathematical formalism does not include multi-pulse effects. On the other hand, HSFL are still controversy discussed, and a universal accepted theory still does not exist yet.

While there are many studies on laser ablation of targets in air to produce LIPSS, similar studies in liquids can only be found in a few [18–20]. These studies report on several differences between LIPSS in air and liquid, one of them being that the periodicity of the LIPSS formed in liquids are found to be several times smaller than those formed in air [19]. An intriguing connection that is yet to be made, lies between LIPSS induced in liquids and the method of pulsed laser ablation in liquids (LAL), which is used to synthesize colloidal nanoparticles from

bulk or pressed-powder [21] targets. LAL has matured to an economically feasible method [22] that found applications in areas ranging from biology [23,24] to laser additive manufacturing [25,26]. While in many LAL-related studies the focus is placed on the effect of the ambient liquid, the utilized laser or the material properties of the ablation target, the surface structure of the target which apparently changes during ablation is generally neglected. However, for aspects such as the nanoparticle productivity [27–29] (i.e. the ablation rate) the surface structure needs to be considered, since the ablation rate is strongly related to the (evolving) optical properties of the target [2]. In other words, if LIPSS are formed on the target, the laser-matter-interaction will change, possibly influencing nanoparticle formation. One of the most important laser parameters in the context of LIPSS formation is the applied laser fluence, it has a tremendous impact on whether LIPSS is formed or not. Typically, a laser fluence close to the ablation threshold leads to distinct LIPSS features while in a high fluence regime LIPSS are often not formed anymore [30,31]. In contrast to LIPSS formation, nanoparticle productivity during LAL increases with higher fluence. Hence, typically the highest possible fluence for a given LAL-setup is utilized for maximum nanoparticle productivity [27,32]. To shed light onto the interplay between LIPSS and LAL and their opposing fluence-trends, LIPSS formation on several metal targets are studied in this study. Due to their relevance in plasmonics [33–35], biomedicine [36,37] and catalysis [38,39] the alloy systems of iron-gold and gold-silver as well as their constituent metals are studied in detail for different fluences and compositions and eventually correlated to nanoparticle productivity.

2. Experimental

In Fig. 1 the experimental setup and a schematic illustration of the process of LAL is shown. The laser pulse interacts with the target and creates a plasma, which consists of ionized and atomized species [40]. During the plasma decay, the energy is transferred to the liquid, which will evaporate the water and form a cavitation bubble. In the cavitation bubble, the formed nanoparticles are confined until the collapse of the cavitation bubble after which the particle will be dispersed into the liquid [1].

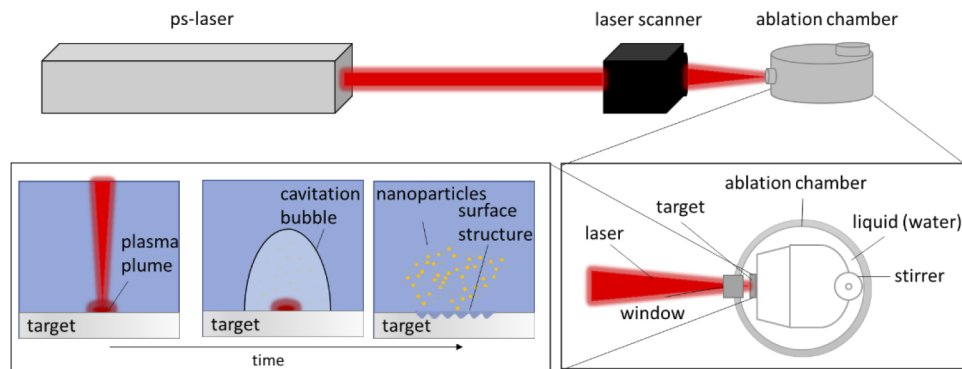


Fig. 1. Schematic illustration of the experimental setup and the process of laser ablation in liquids.

In this study, LAL was performed in water using a picosecond pulsed Nd:YAG laser (Ekspla, Atlantic Series, 10 ps, 100 kHz, 80 μJ , 1064 nm). The laser beam was directed into a laser scanner and focused with an f-theta lens (focal length of 100.1 mm). The laser pulses have a Gaussian intensity distribution profile with laser fluence of 2.7 J/cm^2 if not otherwise noted. The laser beam was scanned on the surface with a scanning speed of 6 m/s for 3 minutes with a focal spot of 63 μm . As shown by Wagner et al, the ablation rate is affected by the lateral interpulse distance.

Laser-induced cavitation bubbles limit the ablation efficiency by scattering and absorption [41]. Therefore, a scanning speed of 6 m/s was chosen, to spatially bypass the laser-induced cavitation bubbles and neglect the influence of the scanning speed. The scanning speed will further influence the periodicity of LIPSS as shown by Zamfirescu et al. With increasing scanning speed, the periodicity of LIPSS is also increased [42]. However, varying the scanning speed and correlating this parameter to LIPSS formation is out of the scope of our study. More information on the LAL setup can be found elsewhere [43]. Additionally, a quarter waveplate was used to change the polarization of the incoming laser-beam from linear to circular (in Section 3.5). Before and after the ablation, the target was weighed, to gravimetrically determine the ablation rate and hence the nanoparticle productivity. The analysis of the LIPSS (morphology and periodicity) after laser ablation is performed with a scanning electron microscope (Philips XL 30 (XL Series), anode voltage: 20 kV). UV-Vis extinction measurements of the collected nanoparticle colloids were carried out with an UV-Vis extinction spectrometer (Thermo Scientific evolution 201) in cuvettes with 1 cm optical path lengths measuring from 1100 nm to 300 nm.

The ablation targets were custom-made by the “Research Institute for Noble Metals and Metal Chemistry”, Schwaebisch Gmuend, Germany and “Vacuumschmelze GmbH & Co. KG”, Hanau, Germany. The density of the materials were either taken from the literature [44,45] or measured with a pycnometer. Targets were polished by the manufacturers; their surface roughness were determined to be $R_a = 180\text{nm} \pm 5.41\text{nm}$ and $R_z = 756\text{nm} \pm 23.4\text{nm}$ as confirmed by confocal microscopy.

In contrary to a damage threshold, the ablation threshold (or also termed as gravimetric ablation threshold in the following) in our experiments is defined as the fluence at which no nanoparticle production can be detected by a gravimetric measurement (i.e. weighing the target before and after ablation), using a scale with an accuracy of 0.1 mg. SEM images of this point confirm that no ablation occurs if we cannot measure a mass difference in the target after processing for 3 minutes.

The reflectivity of selected targets was measured by irradiating the target at a 45° angle and measuring the reflected laser power. The measurement of the power was performed with a power meter containing a pyroelectric detector (FieldMax II -Top, Coherent, Portland (US)). The pyroelectric detector is capable to collect the reflected beam in a sufficient large angle by obtaining the integral power of the reflected beam. For measuring the reflectivity, the probing laser beam had a low laser power to ensure that its power was below any surface modifying power levels. The laser power was measured three times with and without the reflection geometry.

3. Results and discussion

To give an overview of laser-induced surface structures of different metals, Fig. 2 depicts scanning electron microscope (SEM) images of different elemental transition metals and their alloys after ablation with a laser fluence of 2.7 J/cm^2 . Comparing the SEM images, it is evident that alloys of iron with nickel or gold are forming LIPSS while alloys that contain an equimolar amount of silver (i.e. $\text{Fe}_{50}\text{Ag}_{50}$ and $\text{Au}_{50}\text{Ag}_{50}$) are not forming any LIPSS at the applied laser fluences. By assuming that LIPSS formation is due to the excitation of Surface Plasmon Polaritons and by calculating their mean free path, Gnilitzky et al. report that silver is unlikely to form LIPSS for laser wavelengths higher 1030 nm [46], which is in well agreement with our results.

Based on the overview of the surface structure of eight different metals after LAL in Fig. 2, one could assume that an alloy only forms LIPSS if the constituent metals form LIPSS by themselves at the given fluence. It is also clear that LIPSS morphologies, periodicity and width can vary for the shown metals (Fig. 2).

With a laser wavelength of 1064nm, the threshold-periodicity between HSFL and LSFL lies at 532 nm. Taking iron as an example, with a periodicity of $462\text{ nm} \pm 56\text{ nm}$, all the shown materials have a LIPSS-periodicity smaller than 532 nm and are accordingly classified as HSFL.

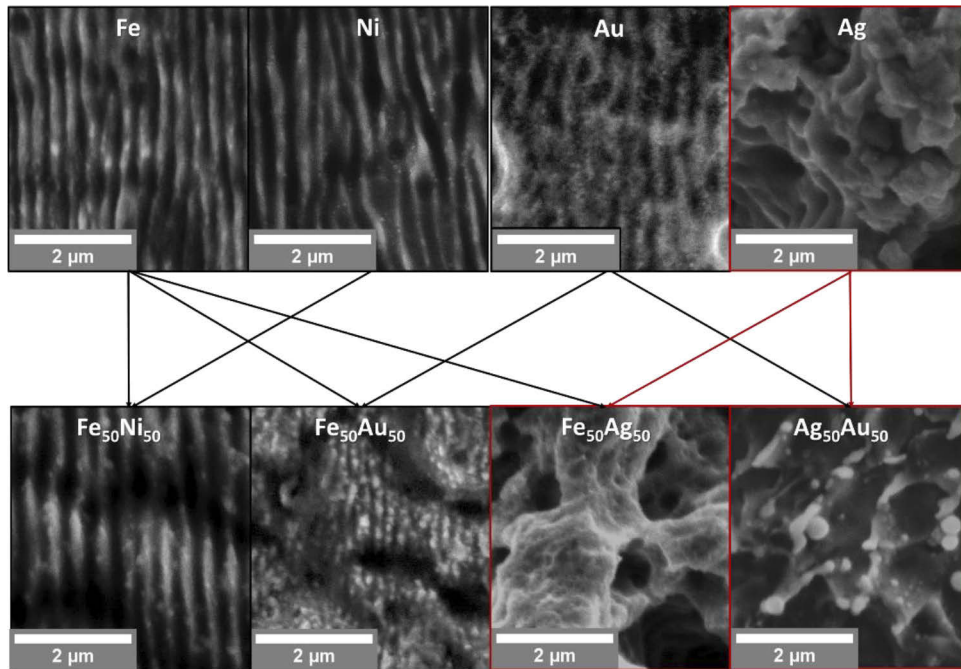


Fig. 2. SEM images of laser-ablated (fluence of 2.7 J/cm^2) elemental metals and their alloys (50:50 composition) in water. Red frames mark metals that didn't form LIPSS while black frames mark the materials that formed LIPSS at the fixed laser parameters.

However, it is evident that the periodicity and width of the LIPSS are material dependent. In the following, the focus is placed on the two different alloy systems, gold-silver, and iron-gold. By studying these materials, we can also study what molar fraction of a LIPSS-forming metal such as gold is needed to form LIPSS when it is alloyed in a solid-solution with a material such as silver, which does not form LIPSS.

3.1. Iron-gold alloy system

Five different iron-gold alloys, i.e. $\text{Fe}_{90}\text{Au}_{10}$, $\text{Fe}_{65}\text{Au}_{35}$, $\text{Fe}_{50}\text{Au}_{50}$, $\text{Fe}_{35}\text{Au}_{65}$, $\text{Fe}_{10}\text{Au}_{90}$, as well as elemental gold and iron were ablated with the given laser parameters. Note that (in contrast to AgAu) the iron-gold system has distinct solubility limits in the phase diagram and the compositions are metastable on the nanoscale at room temperature [47,48]. The resulting surface structures are shown in Fig. 3 while Table 1 summarizes the periodicity and width of the periodic structures. As evident, if the elemental metals form LIPSS, their alloys will also form LIPSS in any compositions. However, the morphology is different for every composition.

The periodicity of the LIPSS does not change significantly for most of the compositions. With a size below 532 nm, all compositions are HSFL. Large differences between the periodicity were not expected, because the elements iron and gold cause already similar LIPSS-periodicities of $462 \text{ nm} \pm 56 \text{ nm}$ and $488 \text{ nm} \pm 45 \text{ nm}$, respectively. As shown in Fig. 4 (left), most of the periodicity data can be described by a constant line at 465nm.

During LIPSS-formation, a target volume is ablated, and nanoparticles are produced. To test if the different morphologies shown in Fig. 3 and quantified in Fig. 4 (left) and Table 1 lead to different nanoparticle productivities, we gravimetrically measured the LAL productivity (i.e. ablated volume per time) for all alloy compositions (Fig. 4, right). The laser-power specific

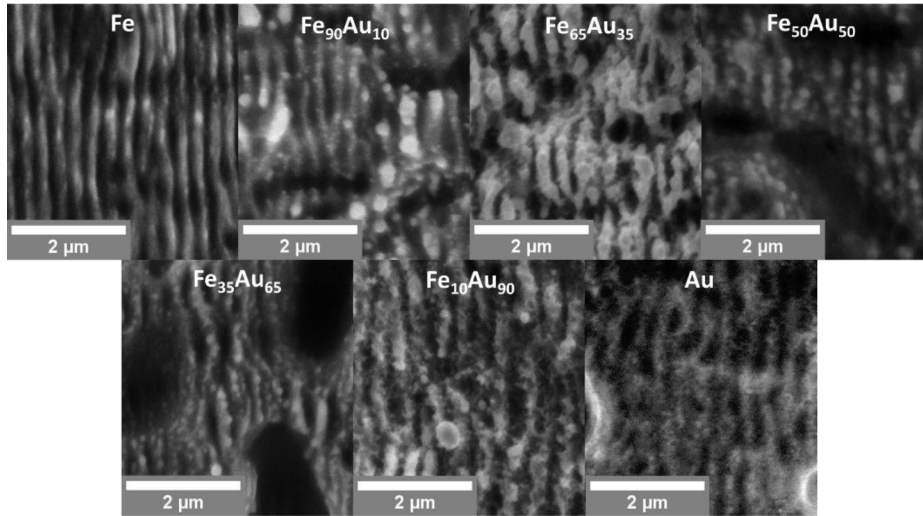


Fig. 3. SEM images showing LIPSS formation after laser ablation (with a fluence of 2.7 J/cm^2) of different iron-gold compositions, as well as elemental gold and iron in water.

Table 1. Density of the targets, mean value of periodicity and width of LIPSS for different FeAu compositions via ps-laser ablation (ablation time: 3 min; wavelength: 1064 nm; fluence: 2.7 J/cm^2 , pulse duration: 10 ps).

Material	Density [g/cm^3]	Periodicity [nm]	Width [nm]
Fe	7.87	462 ± 56	309 ± 61
Fe ₉₀ Au ₁₀	9.02	437 ± 53	237 ± 39
Fe ₆₅ Au ₃₅	11.87	502 ± 37	346 ± 54
Fe ₅₀ Au ₅₀	13.59	447 ± 43	204 ± 24
Fe ₃₅ Au ₆₅	15.30	453 ± 111	172 ± 37
Fe ₁₀ Au ₉₀	18.16	509 ± 70	293 ± 75
Au	19.30	488 ± 45	323 ± 49

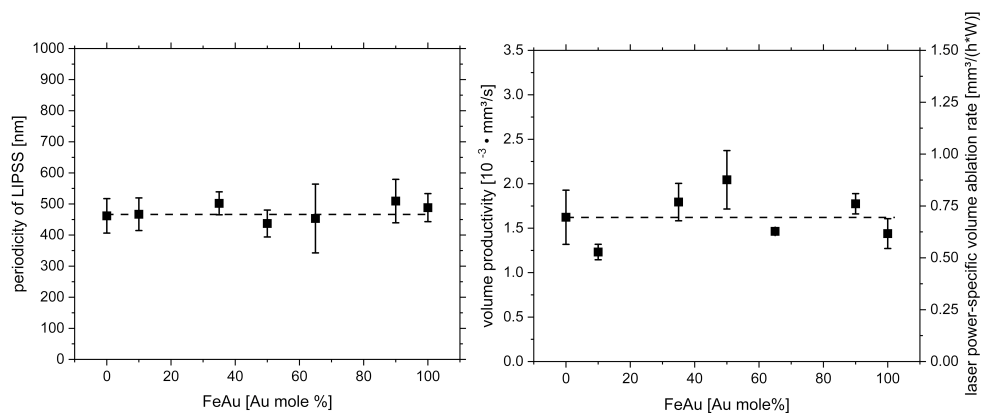


Fig. 4. Left: Periodicity of LIPSS formed after laser ablation of FeAu alloy molar fraction series in water. Right: Volume ablation rate in dependence of the FeAu-alloy composition. Dashed lines are guides to the eye.

volume ablation rate, i.e. the quotient from the volume ablation rate and the laser power, is further shown on the second y-axis for better comparison with the literature.

Within the standard deviation, laser ablation of gold and iron targets lead to similar volume ablation rates of $1.4 \cdot 10^{-3} \text{ mm}^3/\text{s} \pm 0.2 \cdot 10^{-3} \text{ mm}^3/\text{s}$ and $1.6 \cdot 10^{-3} \text{ mm}^3/\text{s} \pm 0.3 \cdot 10^{-3} \text{ mm}^3/\text{s}$, respectively for the given laser system. Accordingly, the laser is ablating similar volumes for all compositions. Because all compositions form LIPSS with nearly the same periodicity, an influence of the LIPSS on the productivity cannot be differentiated.

3.2. Gold-silver alloy system

The gold-silver alloy system consists of one non-LIPSS forming metal (i.e. Ag) and one LIPSS forming material (i.e. Au) for the given fluence of $2.7 \text{ J}/\text{cm}^2$. The ablated surfaces of nine different gold-silver-composition and the elemental metals silver and gold are shown in Fig. 5, while the periodicities and the width of the surface structures are summarized in Table 2. As already shown in Fig. 2, ablation of the equimolar alloy composition does not lead to the formation of LIPSS. From Fig. 5 and Table 2 it is clear, that if the silver content is 50% or higher, there is no LIPSS formation. However, if the LIPSS forming material gold has a molar fraction higher than 60%, then LIPSS formation is observed. Hence in the AgAu system, alloying with Ag or Au can be employed to switch ripple formation off and on.

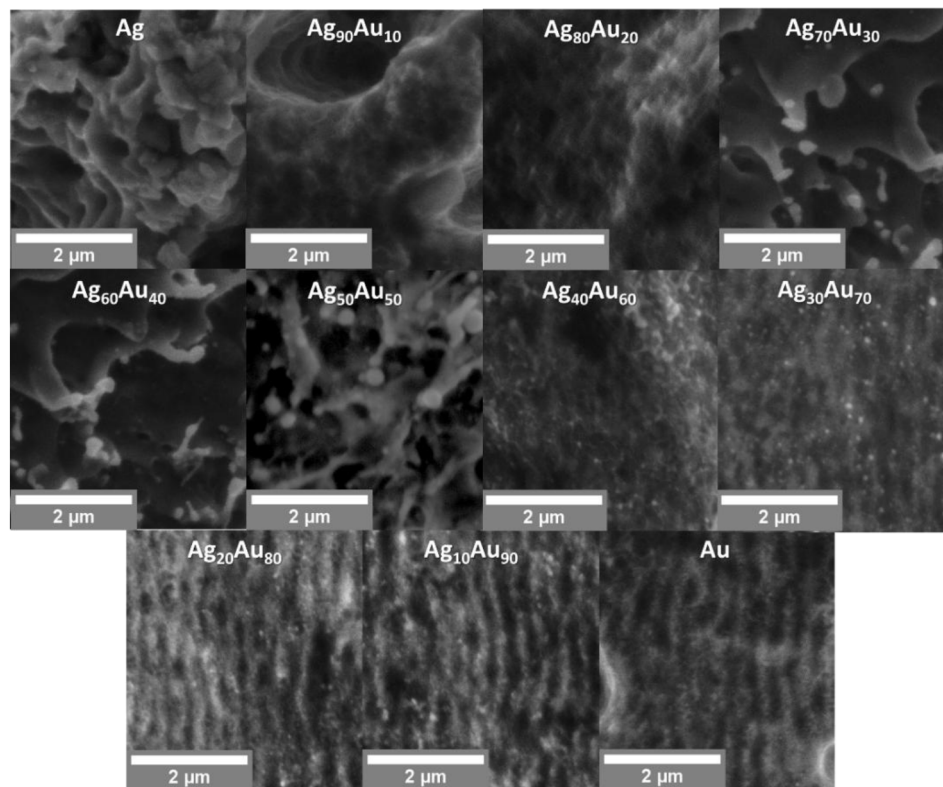


Fig. 5. SEM Images of LIPSS formation, on different gold-silver compositions, as well as elemental gold and silver, after irradiating with a ps-laser (fluence of $2.7 \text{ J}/\text{cm}^2$).

A weak LIPSS-formation already starts for a target with a gold content of 60%. Here, the LIPSS periodicity is $643 \text{ nm} \pm 45 \text{ nm}$. The periodicity decreases linearly until the periodicity of elemental gold is reached (Fig. 6, left). Interestingly, the width of the LIPSS only fluctuates

Table 2. Density of the targets, mean value of periodicity and width of LIPSS for different AgAu compositions via ps-laser ablation (ablation time: 3 min; wavelength: 1064 nm; fluence: 2.7 J/cm², pulse duration: 10 ps).

Material	Density [g/cm ³]	Periodicity [nm]	Width [nm]
Ag	10.50	no LIPSS	-
Ag ₉₀ Au ₁₀	11.00	no LIPSS	-
Ag ₈₀ Au ₂₀	11.55	no LIPSS	-
Ag ₇₀ Au ₃₀	12.16	no LIPSS	-
Ag ₆₀ Au ₄₀	12.85	no LIPSS	-
Ag ₅₀ Au ₅₀	13.61	no LIPSS	-
Ag ₄₀ Au ₆₀	14.48	643 ± 45	351 ± 23
Ag ₃₀ Au ₇₀	15.46	574 ± 22	243 ± 12
Ag ₂₀ Au ₈₀	16.58	560 ± 53	293 ± 28
Ag ₁₀ Au ₉₀	17.85	386 ± 74	279 ± 51
Au	19.30	488 ± 45	323 ± 49

between ± 15% within the whole range of composition (Table 2). Figure 6 shows the volume productivity in dependence of the molar fraction of gold in the gold-silver system. The LAL productivity rises linearly with increasing gold content up to 60%, but above 60% the productivity starts fluctuating or rather decreasing. This point clearly coincides with the alloy composition at which LIPSS formation starts. The decreased (or unsteady) productivity could be explained by the assumption, that the formation of LIPSS consumes laser energy. Instead of transferring the photon energy into the system to ablate the material, a part of the energy is used to form LIPSS. Extrapolating the linear part of Fig. 6 (right) with a linear curve indicates that ablation of a pure gold target would have yielded a productivity of $2.6 \cdot 10^{-3}$ mm³/s if the linear trend would have remained. Hence, one could hypothesize that ~45% of the productivity is lost due to LIPSS formation in this case.

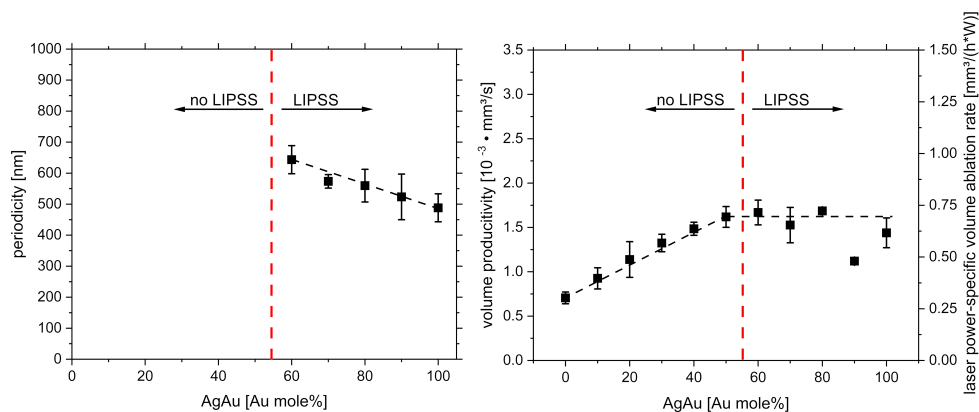


Fig. 6. Left: Periodicity of LIPSS for the different AgAu compositions. Right: Volume ablation rate during LAL in dependence of the composition for AgAu. Dashed lines are guides to the eye.

In contrast to iron, both gold and silver nanoparticles are plasmonic and have a surface plasmon resonance (SPR) peak at the wavelength of 526 nm and 420 nm (Fig. 7). Hence, UV-Vis measurement can be used to detect changes in the properties (i.e. sizes, composition)

of the produced nanoparticles [49]. As shown in Fig. 7, the surface plasmon resonance peak is linearly increasing with the gold molar fraction. Although at Au 60% the LIPSS formation starts, no change in the linear trend and no SPR peak splitting is visible in the SPR peak position. Accordingly, this indicates that the LIPSS formation on the target has no significant influence on the composition of the LAL-produced alloy nanoparticles.

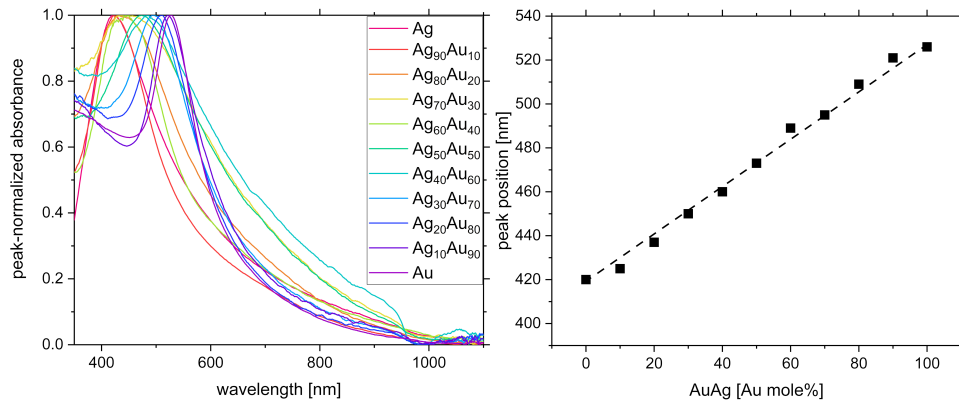


Fig. 7. Left: UV-Vis extinction spectra for different colloidal AgAu compositions. Right: SPR-Peak position in dependence of the molar fraction of Au within the AgAu alloy.

3.3. Influence of laser fluence

Due to the major influence of the laser fluence on the LIPSS formation, in this part its effect on LIPSS and nanoparticle productivity is studied. Figure 2 showed that silver was not forming LIPSS for the used parameters. According to Mesaoudi et al, silver is forming LIPSS for lower fluences close to the gravimetric ablation threshold fluence (their study; employed the following parameters: pulse duration 120 fs; pulse energy 150 μ J; repetition rate 1 kHz; scan velocity 0.05 mm/s) [11]. Here, in a first step, the gravimetric ablation threshold fluence of the studied elemental metals and their equimolar alloys are determined (Fig. 8, left). Furthermore, the change of nanoparticle productivity in dependence of the applied laser fluence is measured (Fig. 8, right).

According to the results shown in Fig. 8, iron has the highest gravimetric ablation threshold fluence (1.16 J/cm²) in water among the studied materials while silver has the lowest gravimetric ablation threshold fluences of 0.14 J/cm². The volume ablation rate in dependence of the fluence follows for all metals, except for silver, fairly well with the so called Neuenschwander function [50], i.e. $dV/dt = A/(2 \cdot F) \cdot \ln^2(F/F_{th})$, with dV/dt being the ablated volume per processing time, “A” being a pre-factor, “F” being the peak fluence and “F_{th}” being the threshold fluence (see Table 3).

The nanoparticle productivity of silver can be more accurately described by a linear fit. As evident in Fig. 8 (right), the trend of FeAu could be described by the logarithmic fit while AgAu rather follows a linear trend. Here the linear trend starts after a fluence of 0.38 J/cm² indicating that LIPSS formation occurs only until this fluence is reached. SEM images are taken for all shown metals after ablation with a fluence of 2.72 J/cm² (which is the fluence already used in the previous sections), a fluence 10% above the respective gravimetric ablation threshold and fluence 60% above the ablation threshold. The results are shown for the elemental metals in Fig. 9 and for the alloys in Fig. 10.

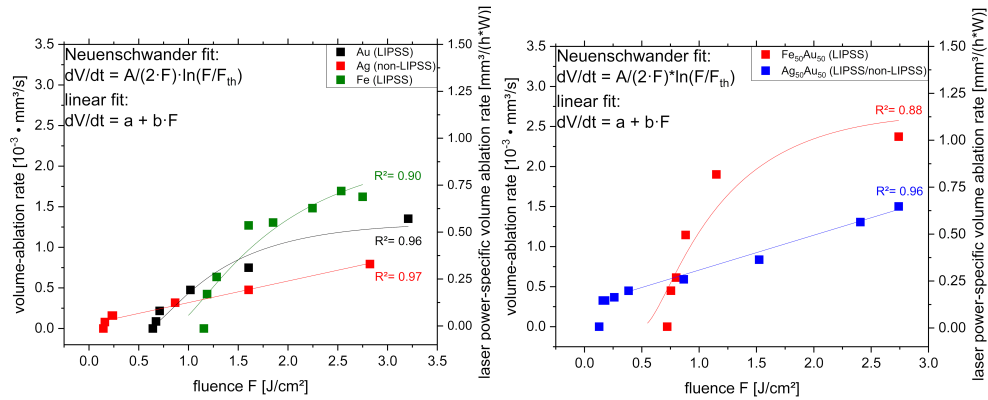


Fig. 8. Volume ablation rate of elemental metals (left) and their equimolar alloys (right) for different fluences F . The y-intercept is taken as the threshold fluence (F_{th}) for the given material. A linear fit was used for non-LIPSS forming materials and the “Neuenschwander” fit was used for LIPSS forming materials.

Table 3. Determined gravimetric ablation threshold fluences of metals shown in Fig. 7 for ps-laser ablation in water

Metal	Threshold fluence [J/cm^2]
Ag	0.14
Au	0.64
Fe	1.16
$\text{Fe}_{50}\text{Au}_{50}$	0.72
$\text{Ag}_{50}\text{Au}_{50}$	0.13

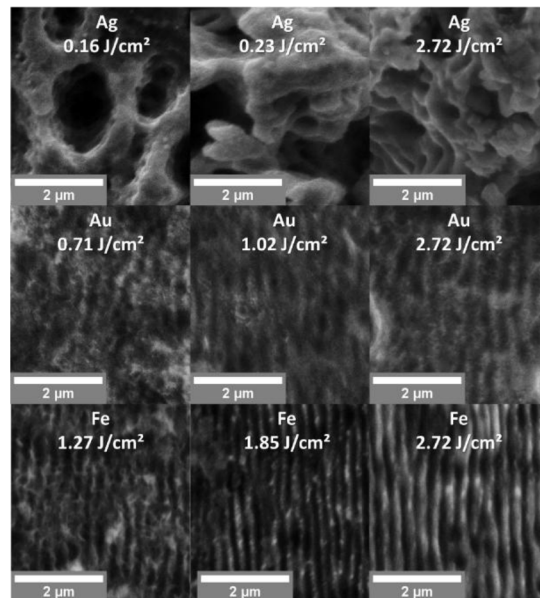


Fig. 9. SEM images of the elemental metals Ag, Au, Fe after ablation with a laser fluence of 10%, 60% above the gravimetric ablation threshold fluence of each metal, and at a fixed fluence of $2.72 \text{ J}/\text{cm}^2$.

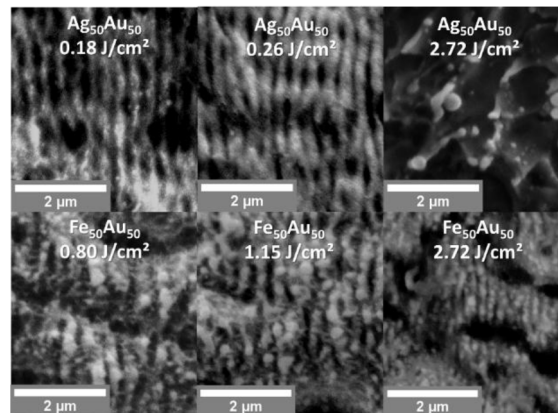


Fig. 10. SEM images of the equimolar AgAu and FeAu alloys after ablation in water with a laser fluence of 10%, 60% above the gravimetric ablation threshold fluence of each alloy, and a fixed fluence of 2.72 J/cm^2 .

Except for Ag and $\text{Ag}_{50}\text{Au}_{50}$, the LIPSS formation is more distinct for each shown metal with increasing fluence. For these materials, at 10% above the gravimetric ablation threshold fluence, the LIPSS is not very pronounced, except for iron. This could be explained with the high gravimetric ablation threshold-fluence of iron (1.16 J/cm^2). In this context, 10% of this fluence is apparently a higher absolute fluence increase than for gold. For ablation of elemental silver, we cannot find any LIPSS formation even at very low fluences. The structures induced at a laser fluence 0.23 J/cm^2 seem similar to the structures induced at 2.72 J/cm^2 . Even at the gravimetric ablation threshold fluence, no LIPSS was found. The structures formed on silver are reported “coral-like structures” in the literature [51]. A special case among the studied materials is evident for the $\text{Ag}_{50}\text{Au}_{50}$ alloy. LIPSS formation was found at 10% (i.e. 0.18 J/cm^2) over the gravimetric ablation threshold fluence and at a fluence 60% above the gravimetric ablation threshold fluence (i.e. 0.26 J/cm^2) the LIPSS was more perceptible. At a higher fluence of 2.72 J/cm^2 , LIPSS cannot be observed as already shown in Fig. 2. By comparing Fig. 10 with Fig. 8, it can be assumed that the nanoparticle productivity trend of a material is indicative for the formation of LIPSS. If LIPSS is formed the nanoparticle productivity follows a second-order logarithmic (“Neuenschwander”) trend like it is the case for ablation of iron and gold. Materials that don’t form LIPSS tend to follow a linear dependence between laser fluence and volume ablation rate. $\text{Au}_{50}\text{Ag}_{50}$ forms LIPSS when ablated with low fluences, while no LIPSS is formed for higher fluences. These results support the result of Fig. 6 which also shows an influence of LIPSS on the nanoparticle productivity. Since depending on the fluence, ablation of $\text{Au}_{50}\text{Ag}_{50}$ can lead to LIPSS or not, this target material was studied in more detail regarding its reflectivity for the incoming laser wavelength. The reflectivity was measured as described in the experimental section. For an unirradiated clean surface, $79.57\% \pm 0.29\%$ of the energy was reflected and could not be absorbed by the material. When the reflectivity measurement is repeated on an area containing LIPSS structures (i.e. $\text{Ag}_{50}\text{Au}_{50}$ that was irradiated with a fluence of 0.9 J/cm^2) only $30.94\% \pm 3.07\%$ of the laser energy was reflected, which indicates an improved absorption behavior through the LIPSS. As Fig. 6 and Fig. 8 indicate a better ablation rate for materials without LIPSS, the reflectivity measurement was conducted on an ablated surface that did not form LIPSS structures, i.e. $\text{Ag}_{50}\text{Au}_{50}$ that was irradiated with a fluence of 2.74 J/cm^2 . For this surface the reflectivity was measured to be $10.39\% \pm 1.06\%$, hence, it is 20% lower than the reflectivity of a surface that showed LIPSS. This finding strongly supports the result, that without LIPSS on the target surface the absorption and the ablation efficiency significantly increases.

To further support this interesting finding which directly relates to nanoparticle productivity, we have extended this study to a further material that is not forming LIPSS structures at a fluence of 2.72 J/cm^2 . Copper is such a material, its volume ablation rate in dependence of the fluence is shown in Fig. 11. As evident, a linear trend occurs after fluences larger than 0.5 J/cm^2 in Fig. 11. For fluences lower than 0.5 J/cm^2 a different trend is evident. Similar to the results obtained for $\text{Ag}_{50}\text{Au}_{50}$, the two trends in the volume ablation rate are indicative of whether LIPSS is formed or not. SEM images of these copper surfaces (Fig. 11) depict LIPSS structure if the surface is ablated with low fluence ($< 0.5 \text{ J/cm}^2$). For higher fluence ($> 0.5 \text{ J/cm}^2$) no LIPSS are evident on the target surface.

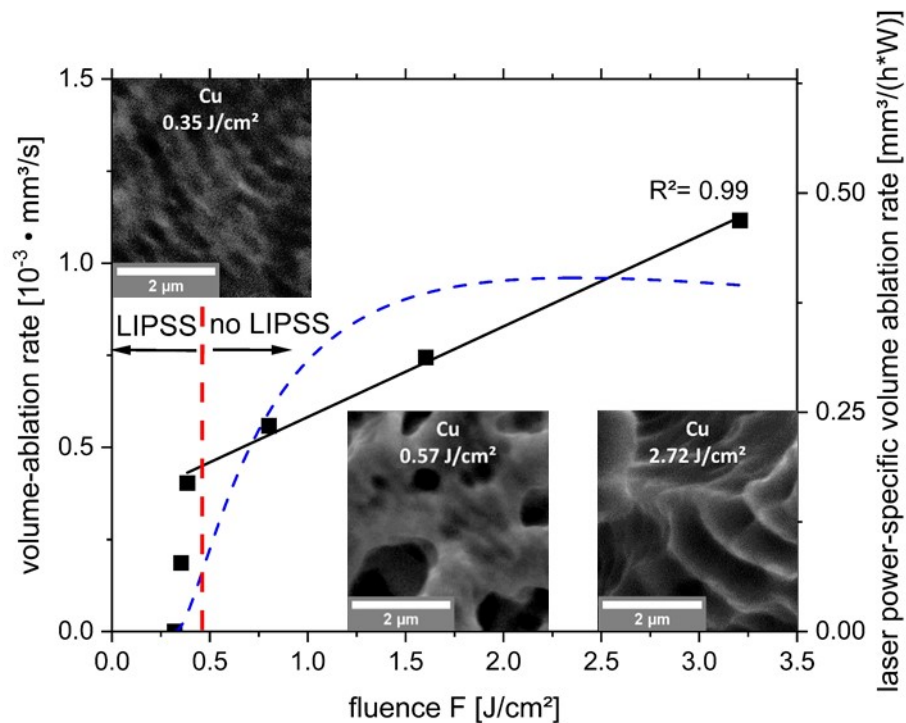


Fig. 11. Measurement of the gravimetric ablation threshold fluence of copper and selected SEM-Images for different ablation fluences (0.35 J/cm^2 , 0.57 J/cm^2 , 2.72 J/cm^2). Two fits are shown for the same data to evaluate their goodness-of-fit. The black fit is a linear fit, while the blue dotted fit is the logarithmic fit described in Fig. 8.

In Fig. 12 the evolution of LIPSS with increasing pulse numbers for the equimolar FeNi target was studied in more detail. In the upper part of the figure, images are shown for a fluence 10% over the threshold fluence (i.e. 0.07 J/cm^2) while the lower part of the figure shows images of the surface after ablation with a high fluence of 2.72 J/cm^2 . In the case of 0.07 J/cm^2 , LIPSS is formed already after the first pulse while for 2.72 J/cm^2 , LIPSS forms after the second pulse. As known from the literature, LIPSS formation is regarded as a process favored by laser fluences close to the ablation threshold [3].

3.4. Influence of LIPSS on the LAL productivity

As shown in the above part, the formation of LIPSS has a distinct influence on the volume ablation rate and the nanoparticle productivity. It can be hypothesized that the nanoparticle

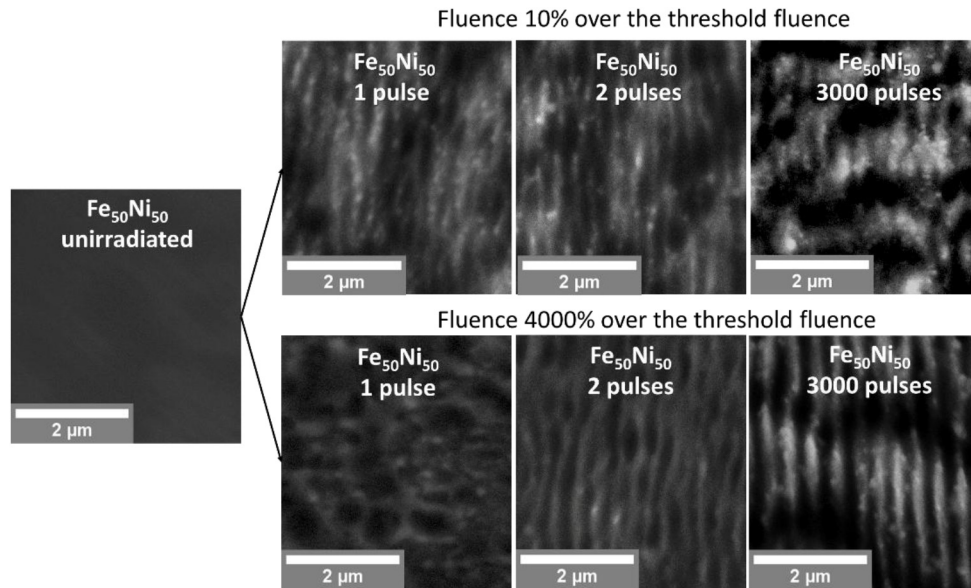


Fig. 12. SEM images of an unirradiated $\text{Fe}_{50}\text{Ni}_{50}$ surface and surfaces after ablation with 1, 2 and 3000 pulses with a fluence 10% (0.07 J/cm^2) over the threshold fluence (top) and a fluence 4000% (2.72 J/cm^2) over the threshold fluence. (bottom)

productivity is higher when LIPSS is not formed during ablation. It is known that a linear laser polarization strongly enhanced the formation of LIPSS. Hence, in this part we want to study the difference between using linearly and circularly polarized light during ablation. To switch the polarization, a quarter waveplate is used. By doing so, LIPSS can be changed or completely turned off. The three equimolar alloys of $\text{Fe}_{50}\text{Ni}_{50}$, $\text{Fe}_{50}\text{Au}_{50}$ and $\text{Ag}_{50}\text{Au}_{50}$ are chosen for this study. The SEM images shown in Fig. 13 summarize the results for ablation with linearly

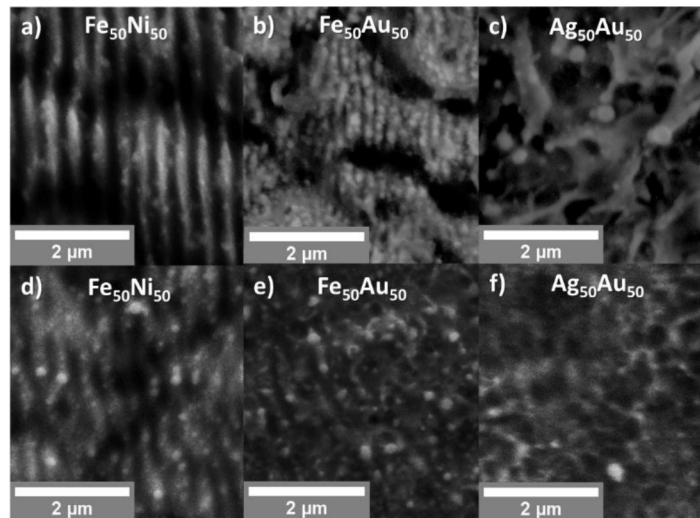


Fig. 13. SEM images of the equimolar alloys after ablation with a fluence of 2.72 J/cm^2 with linearly polarized laser beam [a,b,c] and circularly polarized laser beam [d,e,f].

polarized light Figs. 13(a)–Fig. 13(c) and circularly polarized light Figs. 13(d)–13(f). A change of the surface structures of $\text{Ag}_{50}\text{Au}_{50}$ was not expected because LIPSS formation was not seen in the above experiments conducted with a linear polarized laser. Figure 13(c) and Fig. 13(f) confirm this expectation. For the $\text{Fe}_{50}\text{Au}_{50}$ sample, LIPSS could be turned off effectively by the quarter wave plate (Fig. 13(e)). However, the $\text{Fe}_{50}\text{Ni}_{50}$ sample is still forming weak but evident LIPSS with a circularly polarized beam.

For all three alloys, the ablation rate was determined (Fig. 14). The most significant change is observed for $\text{Fe}_{50}\text{Au}_{50}$, the alloy target material on which the LIPSS could be turned off by circular polarization. Without LIPSS, an increase of 32% in the productivity could be measured. Interestingly, all tested alloys show an increased ablation rate with an increase of 11% for $\text{Fe}_{50}\text{Ni}_{50}$ and an increase of 16% for $\text{Ag}_{50}\text{Au}_{50}$. This could be explained by the higher plasma temperature and electron density caused by the use of a circularly polarized laser beam as recently reported by Wang et al. in the context of laser-induced breakdown spectroscopy [52]. This could effectively result in the higher nanoparticle productivity during LAL. If the effect of this phenomenon (i.e. the use of circularly polarized light) is accounted for with an increase of $\sim 12\%$, this would mean that $\text{Fe}_{50}\text{Au}_{50}$ ablation rate is additionally increased by 20% due to the absence of LIPSS structures. This is in well agreement with the 20% lower reflectivity as measured above.

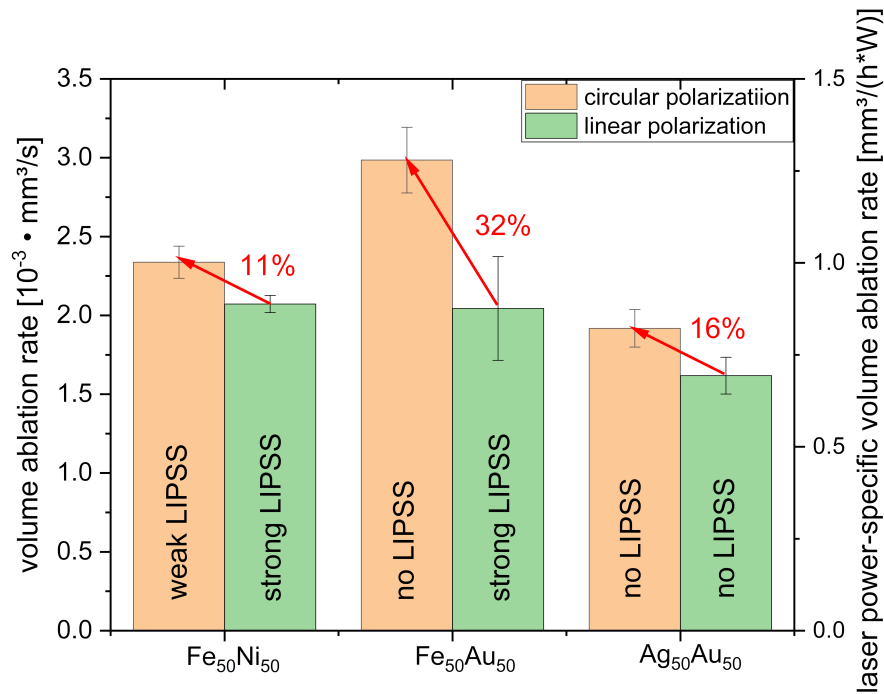


Fig. 14. Volume ablation rate of equimolar alloys after pulsed laser ablation in water with circularly and linearly polarized light (2.7 J/cm^2), respectively.

4. Conclusion

Laser ablation of alloy composition series in liquids is interesting for both alloy nanoparticle applications research such as catalysis [53] or biomedicine [54] or fundamental research on ablation mechanism. Hence, iron, gold, silver and their alloys as well as copper were studied on

their ability to form LIPSS by picosecond pulsed laser ablation in water at a fluence optimized for maximum nanoparticle productivity. It is found that alloys with equimolar ratio will form LIPSS, if the constituent elemental metals also form LIPSS. This result could be confirmed for the pulsed ablation of alloys such as FeNi and FeAu in water. If one of the components does not form LIPSS at a fixed fluence, the equimolar alloy also does not form LIPSS. This could be evidenced by ablation of FeAg and AgAu targets. If the mole fraction of the LIPSS forming metal is increased, the alloy also starts to form LIPSS. Hence, alloys present an elegant route to switch ripple formation on and off. Furthermore, an important correlation between nanoparticle productivity and LIPSS formation could be made. As in the case of the AgAu alloy system, LIPSS can be induced by either changing the composition or by changing the laser fluence. Interestingly, the change between surface structures with or without LIPSS is reflected in the obtained nanoparticle productivity. While nanoparticle productivity shows a linear trend in the volume nanoparticle productivity if no LIPSS is formed on the ablation target (e.g. Ag), a decreased productivity is observed when LIPSS is formed (e.g. Ag₄₀Au₆₀, Ag₃₀Au₇₀, Ag₂₀Au₈₀, Ag₁₀Au₉₀, Au) and laser energy is consumed to form these structures. Reflectivity measurements on a Ag₅₀Au₅₀ target show that if LIPSS is not formed on the target, its reflectivity is decreased by 20%. By turning off LIPSS formation by using a quarter waveplate and changing the linearly polarized beam into a circularly polarized beam, we further successfully applied our findings to increase the productivity of a Fe₅₀Au₅₀ target by 32%. Since LIPSS is typically not formed during LAL with nanosecond lasers, our findings might explain differences in material dependency of nanoparticle productivity trends of LAL with picosecond compared to nanosecond lasers.

Funding

Deutsche Forschungsgemeinschaft (GO 2566/2-1, BA 3580/18-1).

Acknowledgments

We acknowledge support by the Open Access Publication Fund of the University of Duisburg-Essen.

References

1. D. Zhang, B. Gökce, and S. Barcikowski, "Laser Synthesis and Processing of Colloids: Fundamentals and Applications," *Chem. Rev.* **117**(5), 3990–4103 (2017).
2. S. Reich, A. Letzel, B. Gökce, A. Menzel, S. Barcikowski, and A. Plech, "Incubation Effect of Pre-Irradiation on Bubble Formation and Ablation in Laser Ablation in Liquids," *ChemPhysChem* **20**(8), 1036–1043 (2019).
3. J. Bonse, S. Hohm, S. V. Kirner, A. Rosenfeld, and J. Kruger, "Laser-Induced Periodic Surface Structures-A Scientific Evergreen," *IEEE J. Sel. Top. Quantum Electron.* **23**(3), 9000615 (2017).
4. H. M. Vandriel, J. E. Sipe, and J. F. Young, "Laser-Induced Periodic Surface-Structure on Solids - a Universal Phenomenon," *Phys. Rev. Lett.* **49**(26), 1955–1958 (1982).
5. S. Graf and F. A. Muller, "Polarisation-dependent generation of fs-laser induced periodic surface structures," *Appl. Surf. Sci.* **331**, 150–155 (2015).
6. J. Eichstädt, G. R. B. E. Römer, and A. J. H. In't Veld, "Determination of irradiation parameters for laser-induced periodic surface structures," *Appl. Surf. Sci.* **264**, 79–87 (2013).
7. W. Han, L. Jiang, X. Li, P. Liu, L. Xu, and Y. Lu, "Continuous modulations of femtosecond laser-induced periodic surface structures and scanned line-widths on silicon by polarization changes," *Opt. Express* **21**(13), 15505–15513 (2013).
8. J. Bonse, R. Koter, M. Hartelt, D. Spaltmann, S. Pentzien, S. Hohm, A. Rosenfeld, and J. Kruger, "Tribological performance of femtosecond laser-induced periodic surface structures on titanium and a high toughness bearing steel," *Appl. Surf. Sci.* **336**, 21–27 (2015).
9. J. Eichstädt, G. R. B. E. Römer, and A. Huis int Veld, "Towards Friction Control using laser-induced periodic Surface Structures," *Phys. Procedia* **12**, 7–15 (2011).
10. C. Yiannakou, C. Simitzi, A. Manousaki, C. Fotakis, A. Ranella, and E. Stratakis, "Cell patterning via laser micro/nano structured silicon surfaces," *Biofabrication* **9**(2), 025024 (2017).
11. H. Messaoudi, S. Das, J. Lange, F. Heinrich, S. Schrader, M. Frohme, and R. Grunwald, "Femtosecond-Laser Induced Periodic Surface Structures for Surface Enhanced Raman Spectroscopy of Biomolecules," (2015), pp. 207–222.

12. O. Varlamova, J. Reif, M. Stolz, R. Borcia, I. D. Borcia, and M. Bestehorn, "Wetting properties of LIPSS structured silicon surfaces," *Eur. Phys. J. B* **92**(5), 91 (2019).
13. A. R. Neale, Y. Jin, J. L. Ouyang, S. Hughes, D. Hesp, V. Dhanak, G. Dearden, S. Edwardson, and L. J. Hardwick, "Electrochemical performance of laser micro-structured nickel oxyhydroxide cathodes," *J. Power Sources* **271**, 42–47 (2014).
14. C. S. Nathala, A. Ajami, A. A. Ionin, S. I. Kudryashov, S. V. Makarov, T. Ganz, A. Assion, and W. Husinsky, "Experimental study of fs-laser induced sub-100-nm periodic surface structures on titanium," *Opt. Express* **23**(5), 5915–5929 (2015).
15. M. Barberoglou, D. Gray, E. Magoulakis, C. Fotakis, P. A. Loukakos, and E. Stratakis, "Controlling ripples' periodicity using temporally delayed femtosecond laser double pulses," *Opt. Express* **21**(15), 18501–18508 (2013).
16. F. Keilmann and Y. H. Bai, "Periodic Surface-Structures Frozen into Co₂ Laser-Melted Quartz," *Appl. Phys. A: Solids Surf.* **29**(1), 9–18 (1982).
17. J. E. Sipe, J. F. Young, J. S. Preston, and H. M. van Driel, "Laser-induced periodic surface structure. I. Theory," *Phys. Rev. B* **27**(2), 1141–1154 (1983).
18. D. Zhang and K. Sugioka, "Hierarchical microstructures with high spatial frequency laser induced periodic surface structures possessing different orientations created by femtosecond laser ablation of silicon in liquids," *Opto-Electron. Adv.* **2**(3), 19000201–19000218 (2019).
19. C. Albu, A. Dinescu, M. Filipescu, M. Ulmeanu, and M. Zamfirescu, "Periodical structures induced by femtosecond laser on metals in air and liquid environments," *Appl. Surf. Sci.* **278**, 347–351 (2013).
20. T. Kobayashi, T. Wakabayashi, Y. Takushima, and J. Yan, "Formation behavior of laser-induced periodic surface structures on stainless tool steel in various media," *Precis. Eng.* **57**, 244–252 (2019).
21. F. Waag, Y. Li, A. R. Ziefuss, E. Bertin, M. Kamp, V. Duppel, G. Marzun, L. Kienle, S. Barcikowski, and B. Gökce, "Kinetically-controlled laser-synthesis of colloidal high-entropy alloy nanoparticles," *RSC Adv.* **9**(32), 18547–18558 (2019).
22. S. Jendrzey, B. Gökce, M. Epple, and S. Barcikowski, "How Size Determines the Value of Gold: Economic Aspects of Wet Chemical and Laser-Based Metal Colloid Synthesis," *ChemPhysChem* **18**(9), 1012–1019 (2017).
23. C. Streich, S. Koenen, M. Lelle, K. Peneva, and S. Barcikowski, "Influence of ligands in metal nanoparticle electrophoresis for the fabrication of biofunctional coatings," *Appl. Surf. Sci.* **348**, 92–99 (2015).
24. A. Al-Kattan, V. P. Nirwan, A. Popov, Y. V. Ryabchikov, G. Tselikov, M. Sentis, A. Fahmi, and A. V. Kabashin, "Recent Advances in Laser-Ablative Synthesis of Bare Au and Si Nanoparticles and Assessment of Their Prospects for Tissue Engineering Applications," *Int. J. Mol. Sci.* **19**(6), 1563 (2018).
25. C. Donate-Buendia, F. Fromel, M. B. Wilms, R. Streubel, J. Tenkamp, T. Hupfeld, M. Nachev, E. Gökce, A. Weisheit, S. Barcikowski, F. Walther, J. H. Schleifenbaum, and B. Gökce, "Oxide dispersion-strengthened alloys generated by laser metal deposition of laser-generated nanoparticle-metal powder composites," *Mater. Des.* **154**, 360–369 (2018).
26. R. Streubel, M. B. Wilms, C. Donate-Buendia, A. Weisheit, S. Barcikowski, J. H. Schleifenbaum, and B. Gökce, "Depositing laser-generated nanoparticles on powders for additive manufacturing of oxide dispersed strengthened alloy parts via laser metal deposition," *Jpn. J. Appl. Phys.* **57**(4), 040310 (2018).
27. R. Streubel, S. Barcikowski, and B. Gökce, "Continuous multigram nanoparticle synthesis by high-power, high-repetition-rate ultrafast laser ablation in liquids," *Opt. Lett.* **41**(7), 1486–1489 (2016).
28. A. Ionin, A. Ivanova, R. Khmel'nitskii, Y. Klevkov, S. Kudryashov, N. Mel'nik, A. Nastulyavichus, A. Rudenko, I. Saraeva, N. Smirnov, D. Zayarny, A. Baranov, D. Kirilenko, P. Brunkov, and A. Shakhmin, "Milligram-per-second femtosecond laser production of Se nanoparticle inks and ink-jet printing of nanophotonic 2D-patterns," *Appl. Surf. Sci.* **436**, 662–669 (2018).
29. S. Dittrich, R. Streubel, C. McDonnell, H. P. Huber, S. Barcikowski, and B. Gökce, "Comparison of the productivity and ablation efficiency of different laser classes for laser ablation of gold in water and air," *Appl. Phys. A: Solids Surf.* **125**(6), 432 (2019).
30. E. Allahyari, J. J. J. Nivas, M. Valadan, R. Fittipaldi, A. Vecchione, L. Parlato, R. Bruzzese, C. Altucci, and S. Amoruso, "Plume shielding effects in ultrafast laser surface texturing of silicon at high repetition rate in air," *Appl. Surf. Sci.* **448**, 128–133 (2019).
31. T. T. D. Huynh and N. Semmar, "Dependence of ablation threshold and LIPSS formation on copper thin films by accumulative UV picosecond laser shots," *Appl. Phys. A: Solids Surf.* **116**(3), 1429–1435 (2014).
32. R. Streubel, G. Bendt, and B. Gökce, "Pilot-scale synthesis of metal nanoparticles by high-speed pulsed laser ablation in liquids," *Nanotechnology* **27**(20), 205602 (2016).
33. E. Messina, E. Cavallaro, A. Cacciola, R. Saija, F. Borghese, P. Denti, B. Fazio, C. D'Andrea, P. G. Gucciardi, M. A. Iati, M. Meneghetti, G. Compagnini, V. Amendola, and O. M. Marago, "Manipulation and Raman Spectroscopy with Optically Trapped Metal Nanoparticles Obtained by Pulsed Laser Ablation in Liquids," *J. Phys. Chem. C* **115**(12), 5115–5122 (2011).
34. J. Krawinkel, U. Richter, M. L. Torres-Mapa, M. Westermann, L. Gamrad, C. Rehbock, S. Barcikowski, and A. Heisterkamp, "Optical and electron microscopy study of laser-based intracellular molecule delivery using peptide-conjugated photodispersible gold nanoparticle agglomerates," *J. Nanobiotechnol.* **14**(1), 2 (2016).
35. V. Amendola, S. Scaramuzza, S. Agnoli, S. Polizzi, and M. Meneghetti, "Strong dependence of surface plasmon resonance and surface enhanced Raman scattering on the composition of Au-Fe nanoalloys," *Nanoscale* **6**(3), 1423–1433 (2014).

36. S. Schottler, G. Becker, S. Winzen, T. Steinbach, K. Mohr, K. Landfester, V. Mailander, and F. R. Wurm, "Protein adsorption is required for stealth effect of poly(ethylene glycol)- and poly(phosphoester)-coated nanocarriers," *Nat. Nanotechnol.* **11**(4), 372–377 (2016).
37. A. Hatef, B. Darvish, A. Burke, A. Dagallier, and M. Meunier, "Computational characterization of plasma effects in ultrafast laser irradiation of spherical gold nanostructures for photothermal therapy," *J. Phys. D: Appl. Phys.* **49**(10), 105401 (2016).
38. S. A. C. Carabineiro, N. Bogdanchikova, P. B. Tavares, and J. L. Figueiredo, "Nanostructured iron oxide catalysts with gold for the oxidation of carbon monoxide," *RSC Adv.* **2**(7), 2957–2965 (2012).
39. B. Zugic, L. Wang, C. Heine, D. N. Zakharov, B. A. J. Lechner, E. A. Stach, J. Biener, M. Salmeron, R. J. Madix, and C. M. Friend, "Dynamic restructuring drives catalytic activity on nanoporous gold-silver alloy catalysts," *Nat. Mater.* **16**(5), 558–564 (2017).
40. A. Kanitz, M. R. Kalus, E. L. Gurevich, A. Ostendorf, S. Barcikowski, and D. Amans, "Review on experimental and theoretical investigations of the early stage, femtoseconds to microseconds processes during laser ablation in liquid-phase for the synthesis of colloidal nanoparticles," *Plasma Sources Sci. Technol.* **28**(10), 103001 (2019).
41. P. Wagener, A. Schwenke, B. N. Chichkov, and S. Barcikowski, "Pulsed Laser Ablation of Zinc in Tetrahydrofuran: Bypassing the Cavitation Bubble," *J. Phys. Chem. C* **114**(17), 7618–7625 (2010).
42. M. Zamfirescu, M. Ulmeanu, F. Jipa, O. Cretu, A. Moldovan, G. Epurescu, M. Dinescu, and R. Dabu, "Femtosecond Laser Induced Periodic Surface Structures on ZnO Thin Films," *J. Laser Micro/Nanoeng.* **4**(1), 7–10 (2009).
43. S. Barcikowski, T. Baranowski, Y. Durmus, U. Wiedwald, and B. Gökce, "Solid solution magnetic FeNi nanostrand-polymer composites by connecting-coarsening assembly," *J. Mater. Chem. C* **3**(41), 10699–10704 (2015).
44. J. C. Kraut and W. B. Stern, "The density of gold-silver-copper alloys and its calculation from the chemical composition," *Gold Bull.* **33**(2), 52–55 (2000).
45. D. Am and A. Seifert, *Bestimmung thermophysikalischer Daten von Eisen -Nickel -Legierungen im flüssigen Zustand mittels ohmscher Pulsaufheizung Diplomarbeit* (TU Graz, 2019).
46. I. Gnilytskyi, T. J. Derrien, Y. Levy, N. M. Bulgakova, T. Mocek, and L. Orazi, "High-speed manufacturing of highly regular femtosecond laser-induced periodic surface structures: physical origin of regularity," *Sci. Rep.* **7**(1), 8485 (2017).
47. A. Blachowski, K. Ruebenbauer, A. Rakowska, and S. Kac, "Fractal-like behaviour of the BCC/FCC phase separation in the iron-gold alloys," *J. Microsc.* **237**(3), 395–398 (2010).
48. A. Tymoczko, M. Kamp, O. Prymak, C. Rehbock, J. Jakobi, U. Schurmann, L. Kienle, and S. Barcikowski, "How the crystal structure and phase segregation of Au-Fe alloy nanoparticles are ruled by the molar fraction and size," *Nanoscale* **10**(35), 16434–16437 (2018).
49. A. Neumeister, J. Jakobi, C. Rehbock, J. Moysig, and S. Barcikowski, "Monophasic ligand-free alloy nanoparticle synthesis determinants during pulsed laser ablation of bulk alloy and consolidated microparticles in water," *Phys. Chem. Chem. Phys.* **16**(43), 23671–23678 (2014).
50. B. Lauer, B. Jaeggi, and B. Neuenschwander, "Influence of the Pulse Duration onto the Material Removal Rate and Machining Quality for Different Types of Steel," *Phys. Procedia* **56**, 963–972 (2014).
51. P. Fan, M. Zhong, L. Li, T. Huang, and H. Zhang, "Rapid fabrication of surface micro/nano structures with enhanced broadband absorption on Cu by picosecond laser," *Opt. Express* **21**(10), 11628–11637 (2013).
52. Q. Wang, A. Chen, W. Xu, S. Li, Y. Jiang, and M. Jin, "Signal improvement using circular polarization for focused femtosecond laser-induced breakdown spectroscopy," *J. Anal. At. Spectrom.* **34**, 1242–1246 (2019).
53. G. Marzun, A. Levish, V. Mackert, T. Kallio, S. Barcikowski, and P. Wagener, "Laser synthesis, structure and chemical properties of colloidal nickel-molybdenum nanoparticles for the substitution of noble metals in heterogeneous catalysis," *J. Colloid Interface Sci.* **489**, 57–67 (2017).
54. U. Taylor, D. Tiedemann, C. Rehbock, W. A. Kues, S. Barcikowski, and D. Rath, "Influence of gold, silver and gold-silver alloy nanoparticles on germ cell function and embryo development," *Beilstein J. Nanotechnol.* **6**, 651–664 (2015).

DuEPublico

Duisburg-Essen Publications online

UNIVERSITÄT
DUISBURG
ESSEN

Offen im Denken

ub | universitäts
bibliothek

This text is made available via DuEPublico, the institutional repository of the University of Duisburg-Essen. This version may eventually differ from another version distributed by a commercial publisher.

DOI: 10.1364/OE.28.002909

URN: urn:nbn:de:hbz:464-20200604-150803-5

© 2020 Optical Society of America under the terms of the OSA Open Access Publishing Agreement https://www.osapublishing.org/library/license_v1.cfm#VOR-OA